ACS APPLIED MATERIALS & INTERFACES

Research Article

Cite This: ACS Appl. Mater. Interfaces 2018, 10, 27936−27946

www.acsami.org

Rimelike Structure-Inspired Approach toward in Situ-Oriented Self-Assembly of Hierarchical Porous MOF Films as a Sweat Biosensor

Zhengyun Wang, Ting Liu, Muhammad Asif, Yang Yu, Wei Wang, Haitao Wang, Fei Xiao, and Hongfang Liu*

Key Laboratory of Material Chemistry for Energy Conversion and Storage (Ministry of Education), Hubei Key Laboratory of Material Chemistry and Service Failure, School of Chemistry and Chemical Engineering, Huazhong University of Science and Technology (HUST), 1037 Luoyu Road, Wuhan 430074, P. R. China

Supporting Information

ABSTRACT: Surface-supported metal−organic framework (MOF) films hold fantastic promises for viable scientific applications, particularly in sensors and electronic devices. However, slow diffusion, limited mass transfer, and low conductivity hinder the industrial application of MOFs. Herein, we propose a rime-inspired MOF film based on a kind of beautiful natural landscape. To mimic rime architecture, we compare and conclude the intrinsic similarity between natural biomineralization and electrochemical self-assembly of MOFs and used an anodic-induced approach to producing rime-structured MOF architecture. Interestingly, the MOF film with space-filling macro−meso−micropores exhibits remarkable electrochemical sensing performances for simultaneous determination of lactate and glucose, including high sensitivity, excellent selectivity, and a wide linear range in a wide range of pH values. Moreover, this rime-inspired system is able to be applied as a biofunctional human perspiration sensing platform. Our work opens a new horizon for poring on biomimetic rime concept to explore specifically structured MOFs with more diverse functionalities.

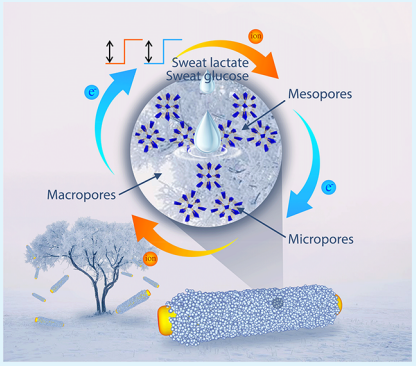

KEYWORDS: *rime-inspired, porous MOFs film, bifunction, non-enzymatic, sweat biosensor*

INTRODUCTION

Fascinating and functionally underpinning metal organic frameworks (MOFs) have opened up a versatile horizon to contrive next generation of optoelectronics, chemical sensors, and energy converters and harvesters, leading us to coin the word "Moftronics" to admire this emerging field.[1−5] The crystalline structure of MOFs is governed by the coordination between the metal ions and an organic linker, engendering MOFs with amazing rational and synthesis versatility and potentiality, and consequently endowed with multiple electrochemical applications.[6,7] Unfortunately, slow diffusion, limited mass transfer, and low conductivity along with low loading of guest molecules are deficiencies that challenge the practical applications of the MOF electrochemical systems.[8,9] On the other hand, numerous MOFs are available only in the form of powders, whereas plenty of potential applications call for thin coatings or films such as MOFs integrated with a carbon substrate.[10,11] In addition, their sizes, morphologies, distributions, and preparation methods also have been proved to remarkably influence their physical and chemical properties.[12−14] Therefore, these abovementioned limitations have motivated researchers to develop more advanced techniques for conductive MOF films or coatings with a charming morphology that may exhibit superior performance, outperforming bulk MOFs. This elegant challenge is still difficult to circumvent because of its uncontrollable modification on substrate surfaces with traditional methods.

Notably, natural structures or materials with sophisticated features can serve as example models to develop materials with excellent performances and characteristics.[15,16] Accordingly, through learning from nature, manipulation of the structure, size, and morphology of MOFs into a nature-inspired configuration can be considered as a pioneering strategy to overcome the inherent weakness of MOF films, leading to the design of new MOF films for unexploited applications. As a kind of rare and distinctive naturally occurring phenomenon, rime is famous for its beautiful appearance. From the microscale viewpoint, rime has high interior porosity, yet a closely packed structure, with the ability to provide an ideal environment to absorb noise and smog. Inspired by the rime's efficient absorption and transport characteristics, we propose a reasonable hypothesis that a rime-structured MOF film would facilitate recognition, diffusion, and adsorption of small biomolecules onto open active sites of MOFs by virtue of the exceptionally high porous structure. It may also offer faster electron transfer, which is suitable for sensing applications. At this point, an interesting question arises: how to prepare

Received: May 13, 2018
Accepted: July 30, 2018
Published: July 30, 2018

DOI: 10.1021/acsami.8b07868
ACS Appl. Mater. Interfaces 2018, 10, 27936−27946

Scheme 1. Fabrication Processes of the ACF-rGO/Cu(INA)$_2$ Electrode

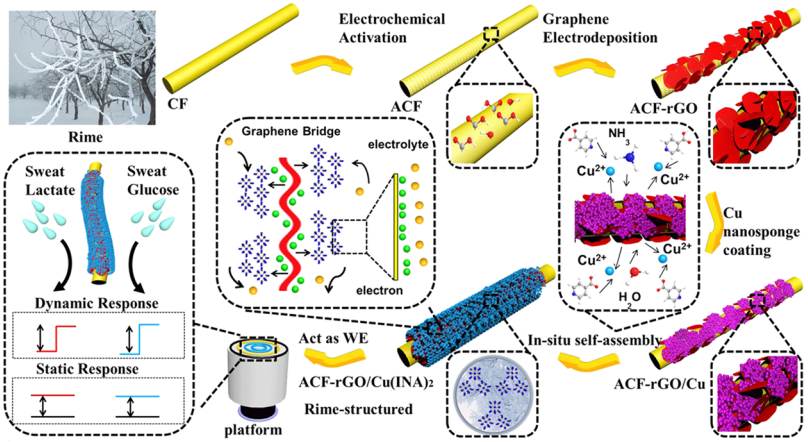

nanoscale rime-structured MOF films? Previously, considerable efforts such as the hydrothermal method,[17] microwave approach,[18] monolayer self-assembly fabrication,[19] liquid-phase epitaxy process,[20] evaporation-driven technique,[21] and gel-layer syntheses[22] were devoted to fabricate surface-supported MOF thin films. Given that these methods are noncontrollable for the fabrication of films with a uniform porous morphology on a substrate, an attractive thinking would be that nanoscale rime-structured MOF films need to be directionally self-assembled through a facile, manageable, and mild technique. We are still seeking inspiration from nature. Vast majority of living organisms construct molecular architectures with a specific porous design to provide structural support or an exoskeletal protection soft tissue.[23] This self-assembly formation process regulated with the exquisite control of crystal compositional specificity, size, distribution, and morphology under physiological conditions is termed biomineralization.[24] With regard to biomineralization, there is an intrinsic similarity with the process of electrochemical anodic-induced self-assembly of MOF crystals on a substrate. The whole transformation can be compared and understood as follows: (I) an organized microenvironment is constructed to ensure position of the nucleation and determine the type of formative crystals; (II) precise identification and self-assembly of molecules occur at the interface of support; (III) the morphology, size, orientation, and structure of the crystals are regulated by chemical vectors and initially assembled into subunits; and (IV) after further growth, modulation, and epitaxy, the initially assembled subunits form a final multilevel structure. On the basis of these comparisons and summaries, we envision that nanoscale rime-structured MOFs can spontaneously form via an electrochemical self-assembly approach.

Herein, we report a biomimetic rime-structured MOF microelectrode via the electrochemical anodic interface-induced approach toward nonenzymatic sweat biosensors, denoted as **ACF-rGO/Cu(INA)$_2$**, as shown in Scheme 1. To mimic the morphology, we use a simple technique that involves constructing a graphene skeleton-wrapped, activated carbon fiber (ACF) as a patterned axis and electrochemically depositing Cu nanosponge on the surface of a three-dimensional (3D) graphene network and using it to induce the in situ self-assembly of rime-structured Cu(INA)$_2$ on a flexible skeleton. Such a nanorime MOF film with coadjacent channels provides an enhanced electron and mass exchange and transfer in electrochemical reactions because of hierarchical length scale spanning. One charming finding is that the rime-structured Cu(INA)$_2$ film exhibits excellent sensing performances toward lactate as well as glucose, whereas new sensing functions of Cu-based materials have not been discovered.[25,26] Compared with those materials modified with the enzyme, the results have shown that this rime-inspired system exhibits high long-term stability, excellent recoverability, miniature size, and superb electrochemical sensing performances toward perspiration lactate and glucose, giving opportunities for the instantaneous measurement of sweat even if rolled up, incorporated, and folded into the subminiature sweat sensor device, ultimately paving the way toward new generation of MOF-based wearable devices.

EXPERIMENTAL SECTION

Synthesis of the Nanorime ACF-rGO/Cu(INA)$_2$. Carbon fiber (CF) was first cleaned by distilled water. A constant-potential step (3 V) was chosen for the electrochemical activation of the CF. The whole activation was run for 5 min in mixed HNO_3 and H_2SO_4 (volume ratio 1:1). After washing with deionized water, the ACF was obtained. Graphene oxide (GO) prepared from graphite powder, with the modified Hummer's method, was mixed with a certain amount of Na_2SO_4 to obtain an electrolyte. A standard three-electrode system using a thin Pt wire, saturated calomel electrode (SCE), and ACF as the counter electrode, the reference electrode, and the working electrode, respectively, was used for the electrodeposition of reduced GO (rGO). The whole electrodeposition was carried out in the suspension at −0.8 V versus SCE for 5 min. After that, ACF-rGO was obtained. Then, a constant-potential step (−0.35) versus SCE was selected for Cu nanosponge electrodeposition on ACF-rGO. The whole process was run in 0.01 M $Cu(NO_3)_2$ aqueous solution with 1 mM Na_2SO_4 and 1 mM HNO_3 for 10 min to obtained the middle product, denoted as ACF-rGO/Cu. The electrolytes used for the in situ synthesis of Cu(INA)$_2$ MOFs are the following: 900 mg of isonicotinic acid (HINA) was dissolved in 10 mL of dimethylformamide/water/ammonia water (50:40:10 vol %) as the electrolyte for deposition of Cu(INA)$_2$. The depositions were carried out in a two-electrode system with a working electrode (ACF-rGO/Cu) and a counter electrode (a platinum wire) at 2.7 V for 3 min. After washing with distilled water, the obtained product is denoted as **ACF-rGO/Cu(INA)$_2$**.

Material Characterization. X-ray diffraction (XRD) was performed on a Bruker D8 ADVANCE X-ray diffractometer (Cu Kα radiation and a Ni filter) (40 kV, 200 mA). X-ray photoelectron spectroscopy (XPS) was carried on a VG MultiLab 2000 Instrument. The field-emission scanning electron microscope used was a Hitachi X-660 instrument. The electrochemical method for the synthesis was

DOI: 10.1021/acsami.8b07868
ACS Appl. Mater. Interfaces 2018, 10, 27936−27946

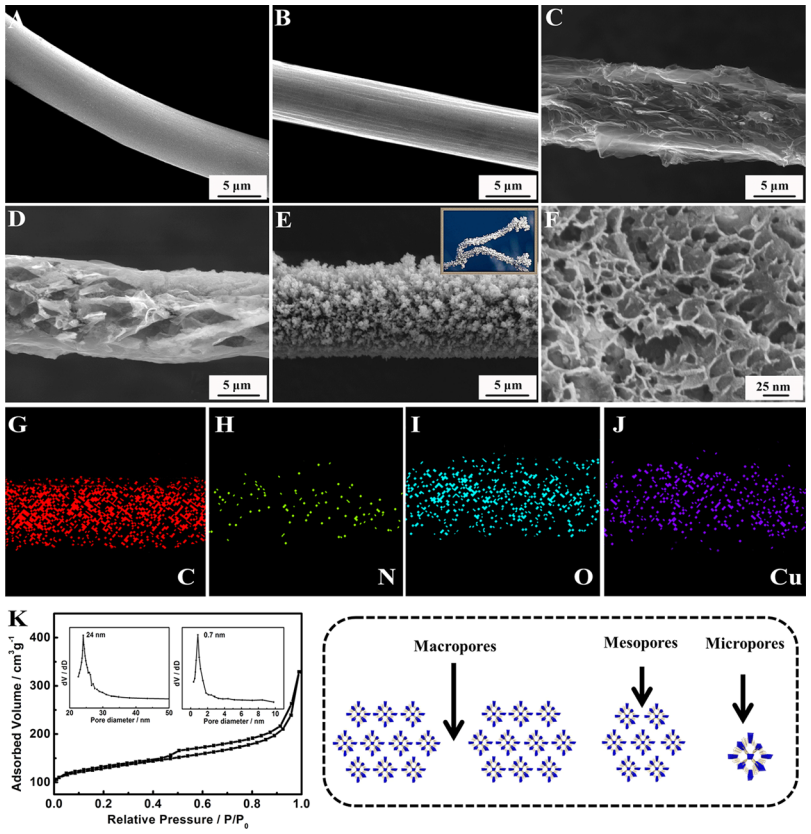

Figure 1. Top-sectional SEM micrographs of (A–D) CF, ACF, ACF-rGO, and ACF-rGO/Cu, respectively, and (E,F) **ACF-rGO/Cu(INA)$_2$**. (G–J) SEM mapping images of ACF-rGO/Cu(INA)$_2$. (K) N_2 isothermal adsorption–desorption curves for **ACF-rGO/Cu(INA)$_2$** and its pore size distribution (left); three kinds of pores in **ACF-rGO/Cu(INA)$_2$** (right).

carried out on the CHI760 electrochemical workstation equipped with a SCE, Pt wire, and nanohybrid as the reference, counter, and working electrodes, respectively, in a typical three-electrode system. Ag/AgCl, Pt, and **ACF-rGO/Cu(INA)$_2$** as the reference, counter, and working electrodes were equipped for electrochemical measurement tests.

RESULTS AND DISCUSSION

Figure 1A displays the scanning electron microscopy (SEM) image of a single smooth CF. After electrochemical activation, as displayed in Figure 1B, the smooth surface of the ACF becomes relatively rough because some oxygen groups including −COOH and −OH are introduced on the surface of the CF, which enriches the active sites and is in favor of the construction of the rGO 3D network. During the network self-assembly, GO nanosheets gradually lose oxygenated groups and are further deposited onto the ACF surface. The genesis of continuous porous architecture lurks in strong $\pi-\pi$ stacking interactions and weak electrostatic repulsions. After electrodeposition of rGO nanosheets, well-defined and interconnected 3D porous graphene network entirely covered the surface of ACF (Figure 1C), conductive to MOFe self-assembly and film-formation.[27] The spongelike Cu covers the pore wall of rGO via electrodeposition, which is used as the metal source for interfacial induction to deposit the MOF film (Figure 1D). As shown in Figure 1E, Cu(INA)$_2$ was in situ self-assembled on ACF-rGO by anodic dissolution from their precursor solutions to form a 3D rime structure (see crystal structures of Cu(INA)$_2$, Figure S1 in the Supporting Information). During the process of anodic dissolution, rime-structured Cu(INA)$_2$ anchored on the 3D skeleton possesses a uniform and close-packed distribution. A large area of macropores with open 1 μm diameter is clearly observed across the rims of compact islands. These snowlike islands are found to be built from a mesoporous film, and a uniform mesoporous nanosheet can be clearly observed under higher magnification. Also, the average size of the mesopores is 25 nm (Figure 1F). The SEM mapping of C, N, O, and Cu elemental distributions also illustrates uniform rime-structured Cu(INA)$_2$ throughout the entire surface of the 3D graphene network (Figure 1G–J). According to previous reports,[28−30] the formation mechanism for modeling biological mineralization of a rime-structured Cu(INA)$_2$ film can be ascribed to the following four sections: initial nucleation, growth of Cu(INA)$_2$ islands, intergrowth, and detachment. In an organized microenvironment, under a relative positive applied potential, the Cu nanosponge begins to lose electrons and dissolve in the solution. Because of the surrounded HINA, automatic identification and self-assembly guarantees that the crystals nucleate on the 3D skeleton surface. Next, after the first nuclei is formed, new Cu(INA)$_2$ crystals start to nucleate adjacent to the existing ones and gradually form interconnected Cu(INA)$_2$ islands. By virtue of the relative large current resistance through the Cu(INA)$_2$ crystals, the current density across the Cu nanosponge is higher. This result directly leads to a tendency of new Cu(INA)$_2$ crystals forming next to them. Then, fresh crystals proceed to nucleate; meanwhile, those already nucleated continue to grow as a film on the surface, next to, and on top of each other, forming a compact layer. Moreover, mesopores is created in the compact layer by virtue of the porosity of the Cu spongy structure (Figure 1F).

DOI: 10.1021/acsami.8b07868
ACS Appl. Mater. Interfaces 2018, 10, 27936−27946

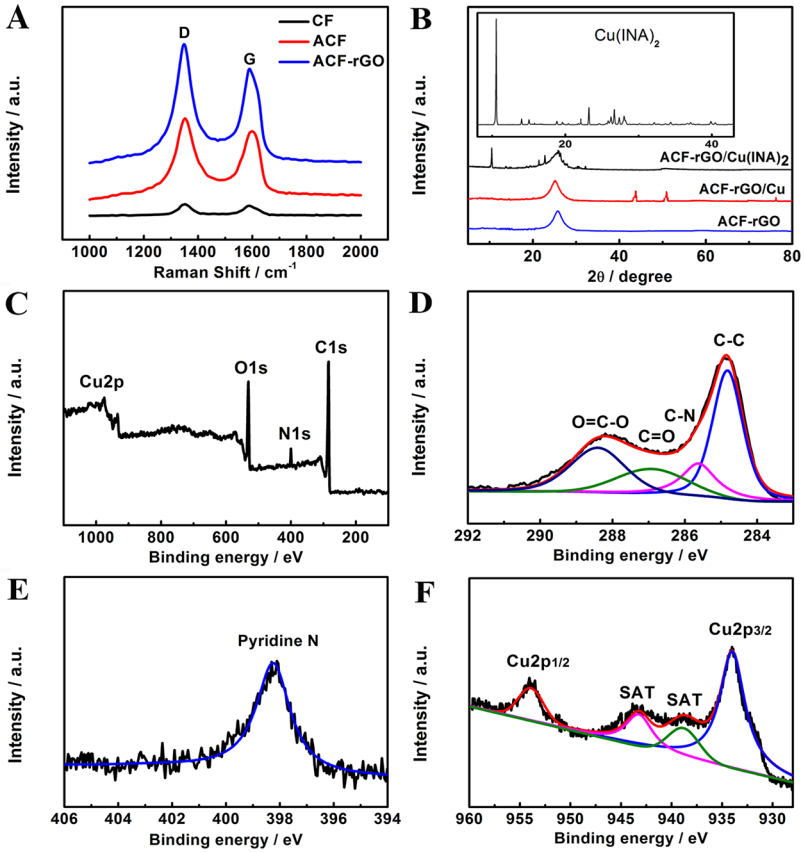

Figure 2. (A) Raman spectra of CF, ACF, and ACF-rGO. (B) XRD of ACF-rGO, ACF-rGO/Cu, and **ACF-rGO/Cu(INA)$_2$**. The inset is Cu(INA)$_2$. (C) XPS spectrum of **ACF-rGO/Cu(INA)$_2$**. (D–F) Curve fit of C 1s, N 1s, and Cu 2p spectra.

Electrochemical methods to synthesize Cu(INA)$_2$ are self-closing in a dendritic mode because Cu(INA)$_2$ tends to wrap up the entire Cu still exposed but does not grow. With further dissolving of the Cu nanosponge, the sponge structure induces the macroporous layer growth to become favored over the non-Cu(INA)$_2$-covered counterparts of the microelectrode. The fact that Cu^{2+} ion concentration is higher in these areas is favorable for the new nucleation and the growth of intergrown crystals and eventually forms an oriented rimelike structure. Finally, some small parts of the Cu(INA)$_2$ layer lose contact with ACF-rGO, driven by the internal stress and undercut of Cu(INA)$_2$. In the whole process, sponge-structured Cu plays the role of metal source; the positive applied potential can be regarded as the chemical vector; the ACF-encapsulated 3D graphene network provides a stable and ideal support to finish the oriented in situ self-assembly of the rime-structured MOF film. The results of porosity textural properties and specific surface area of **ACF-rGO/Cu(INA)$_2$** nanorime measured by N_2 sorption isotherms are summarized in Figure 1K. The specific surface area of **ACF-rGO/Cu(INA)$_2$** is 418.2 $m^2\ g^{-1}$. The type IV isotherms demonstrate the mesoporous structure of **ACF-rGO/Cu(INA)$_2$**. Also, Cu(INA)$_2$ itself contains micropores. The inset of Figure 1K exhibits the pore size distribution of **ACF-rGO/Cu(INA)$_2$**, in which the peaks are mainly centered at 24 and 0.7 nm, corresponding to the closely packed mesopores and micropores in the MOF film.

Raman measurement (Figure 2A) is performed to determine the graphitic structures of CF, ACF, and ACF-rGO samples. The CF displays two well-documented peaks at 1355 and 1595 cm^{-1}, consistent with the respective D-band and G-band. However, I_D/I_G of ACF increases compared with that of the CF, illustrating that more oxygen functional groups onto the ACF surface were introduced after electrochemical activation. A 5-fold enhancement of the Raman signal from ACF was displayed in ACF-rGO. This result can be ascribed to the fact that a great deal of porous graphene nanosheets leads to a large number of marginal areas, resulting in more exposed defects.[31]

The XRD patterns of ACF-rGO, ACF-rGO/Cu, and **ACF-rGO/Cu(INA)$_2$** are shown in Figure 2B. ACF-rGO displays a diffraction peak of (002) diffraction. Besides the broad peak at 25° of the ACF-rGO, the XRD of ACF-rGO/Cu shows three characteristic peaks of Cu at 2θ values of about 43.5°, 50.5°, and 74.3° corresponding to (111), (200), and (220) planes, respectively, which is consistent with previous reports,[32] illustrating the electrodeposition of Cu metal on the substrate surface. For **ACF-rGO/Cu(INA)$_2$**, three peaks at 10.7°, 21.6°, 22.8° associated with (001), (011), and (111) planes, respectively, indicate the successful conversion of Cu(INA)$_2$ from Cu on 3D porous graphene-wrapped ACF through anodic dissolution. **ACF-rGO/Cu(INA)$_2$** was further investigated by XPS. As shown in Figure 2C, Cu 2p, oxygen (O 1s, 530.1 eV), carbon (C 1s, 284.5 eV), and nitrogen (N 1s, 399.5 eV) signals are present in **ACF-rGO/Cu(INA)$_2$**. In Figure 2D, the C 1s peak of **ACF-rGO/Cu(INA)$_2$** reveals several types of carbon bonds: C–C (284.5 eV), C–N (285.8 eV), C═O (286.9 eV), and O–C═O (289.3 eV). The peaks associated with C–N, C═O, and O–C═O originate from Cu(INA)$_2$, and the peak assigned to C–C is predominant. N 1s can be in good agreement with pyridine N with the binding energy located at 398.4 eV (Figure 2E). As shown in Figure 2F, the

DOI: 10.1021/acsami.8b07868
ACS Appl. Mater. Interfaces 2018, 10, 27936–27946

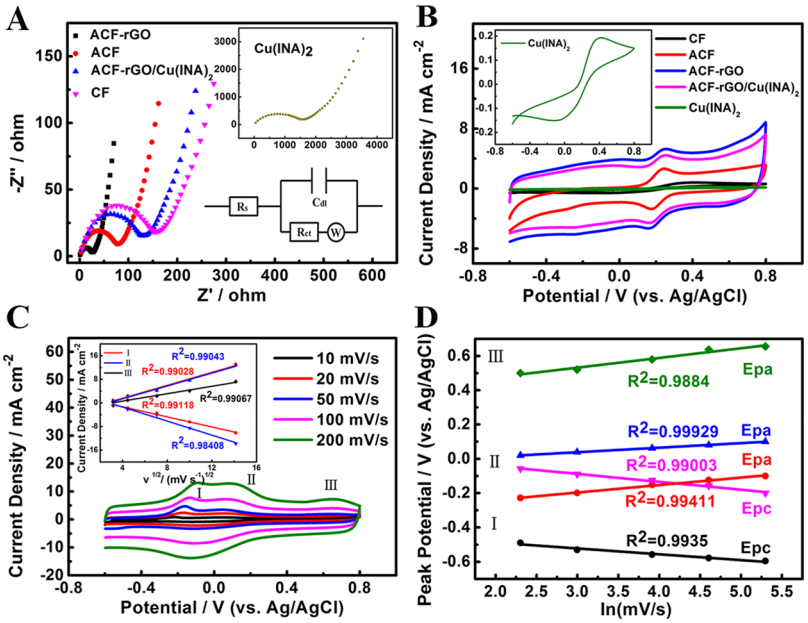

Figure 3. (A) Nyquist plots (frequency range: 0.1−10^5 Hz) and (B) CV curves (scan rate: 50 mV s^{-1}) of CF, ACF, ACF-rGO, bulk $Cu(INA)_2$, and **ACF-rGO/Cu(INA)$_2$** in 0.1 M NaCl with 1.0 mM $K_3Fe(CN)_6$ and 1.0 mM $K_4Fe(CN)_6$. (C) CVs of **ACF-rGO/Cu(INA)$_2$** in simulated sweat at different scan rates (pH = 8.0). The inset is the relationship between the peak current and the square root of the scan rate. (D) Linear fitting of peak potential vs natural logarithm of the scan rate (ln v).

peaks assigned to Cu $2p_{3/2}$ and Cu $2p_{1/2}$ centered at 933.6 and 953.8 eV, respectively, are in consistent with the Cu-MOFs studied previously.[33] Cu 2p also exhibits two satellite peaks at 943.6 and 938.5 eV. The C, H, N, O, and Cu element mass percentages of the as-prepared nanohybrid are 68.03, 1.56, 5.45, 12.46, and 12.50%, respectively, as measured by elemental analysis characterization.

Electrochemical Behavior of the Hybrid Microelectrode. To better understand the electrochemical performances, a $[Fe(CN)_6]^{3-/4-}$ redox probe is first adopted to characterize the electrochemical behavior of **ACF-rGO/Cu(INA)$_2$** as well as of materials including CF, ACF, ACF-rGO, and bulk $Cu(INA)_2$. Figure 3A displays the electrochemical impedance spectroscopy (EIS) results of contrastive samples. The CF exhibits a large faradaic charge-transfer resistance (R_{ct}) of 155 Ω, reducing to 90 Ω for ACF because functional groups were introduced onto its surface for producing pseudocapacitance, and its surface area simultaneously increases. Notably, R_{ct} further decreases to 30 Ω on introducing the 3D graphene network around the ACF. This result indicates an enhanced electron transfer and increased electrochemically active surface areas (ECSAs). It attributes that two-dimensional rGO nanosheets can function as a freestanding array and provide conductive pathways. Bare bulk $Cu(INA)_2$ displays a huge R_{ct}, which reduces to 125 Ω in **ACF-rGO/Cu(INA)$_2$** (see preparation of bulk $Cu(INA)_2$ in the Supporting Information). It is attributable to the fact that the rime structures are successive and linked up, which act as electron transportation bridges between the internal surface and the external circuit of $Cu(INA)_2$. Furthermore, the ECSAs of contrastive electrodes were calculated by the $[Fe(CN)_6]^{3-/4-}$ redox couple based upon Randles−Sevcik equation,[34] $i_p = 2.69 \times 10^5 n^{3/2} A D^{1/2} v^{1/2} c$ ($D = 6.3 \times 10^{-6}$ cm·s^{-1}). As observed in Figure 3B, the cyclic voltammetry (CV) curves display a pair of obvious redox peaks assigned to the one-electron quasi-reversible redox couple (vs Ag/AgCl). The ECSA values are 0.040, 0.17, 0.56, 1.11, and 0.93 cm^2 for bulk $Cu(INA)_2$, CF, ACF, ACF-rGO, and **ACF-rGO/Cu(INA)$_2$**, respectively. Evidently, the ECSA value of ACF-rGO is 2 times as large as that of ACF, suggesting that the 3D rGO network effectively enlarges the ECSA of ACF. Also, **ACF-rGO/Cu(INA)$_2$** possesses a much larger ECSA value in comparison to bulk $Cu(INA)_2$. Moreover, for the bare bulk $Cu(INA)_2$, the wider peak potential separation (ΔE_p, 400 mV) and the relatively smaller peak current (i_p) manifest its poor ECSAs and slow charge-transfer ability. A reduced ΔE_p of 82 mV and an improvement in the peak current are clearly displayed in the resultant **ACF-rGO/Cu(INA)$_2$**. These results indicate that highly conductive and electrocatalytically active ACF-rGO as well as the rime structure of $Cu(INA)_2$ play a momentous part in enhancing the ECSA and electron-transfer rate.

To obtain various electron-transfer parameters of **ACF-rGO/Cu(INA)$_2$**, CV was carried out in simulated sweat at different potential scan rates (Figure 3C). Well-defined redox peaks at −0.15 and −0.55, 0.15 and −0.1, and 0.62 V (vs Ag/AgCl) can be assigned to the interconversion between Cu(0)/Cu(I), Cu(I)/Cu(II), and Cu(II)/Cu(III), respectively. For peaks I and II, the increasing anodic (E_{pa}) and cathodic (E_{pc}) peak potentials shift to more positive and negative, respectively, as the scan rate increases, signifying a quasi-reversible conversion. For peak III, conversion of the Cu(II)/Cu(III) couple can be regarded as a nonreversible process because of the unconspicuous cathodic peak. In addition, the magnitudes of anodic (I_{pa}) and cathodic (I_{pc}) peak currents are linear functions of the square root of scan rate, implying a diffusion-controlled electrochemical process (inset, Figure 3C). On the basis of Laviron's theory,[35] the electron-transfer number (n) and the electron-transfer coefficient (α) are calculated

DOI: 10.1021/acsami.8b07868
ACS Appl. Mater. Interfaces 2018, 10, 27936−27946

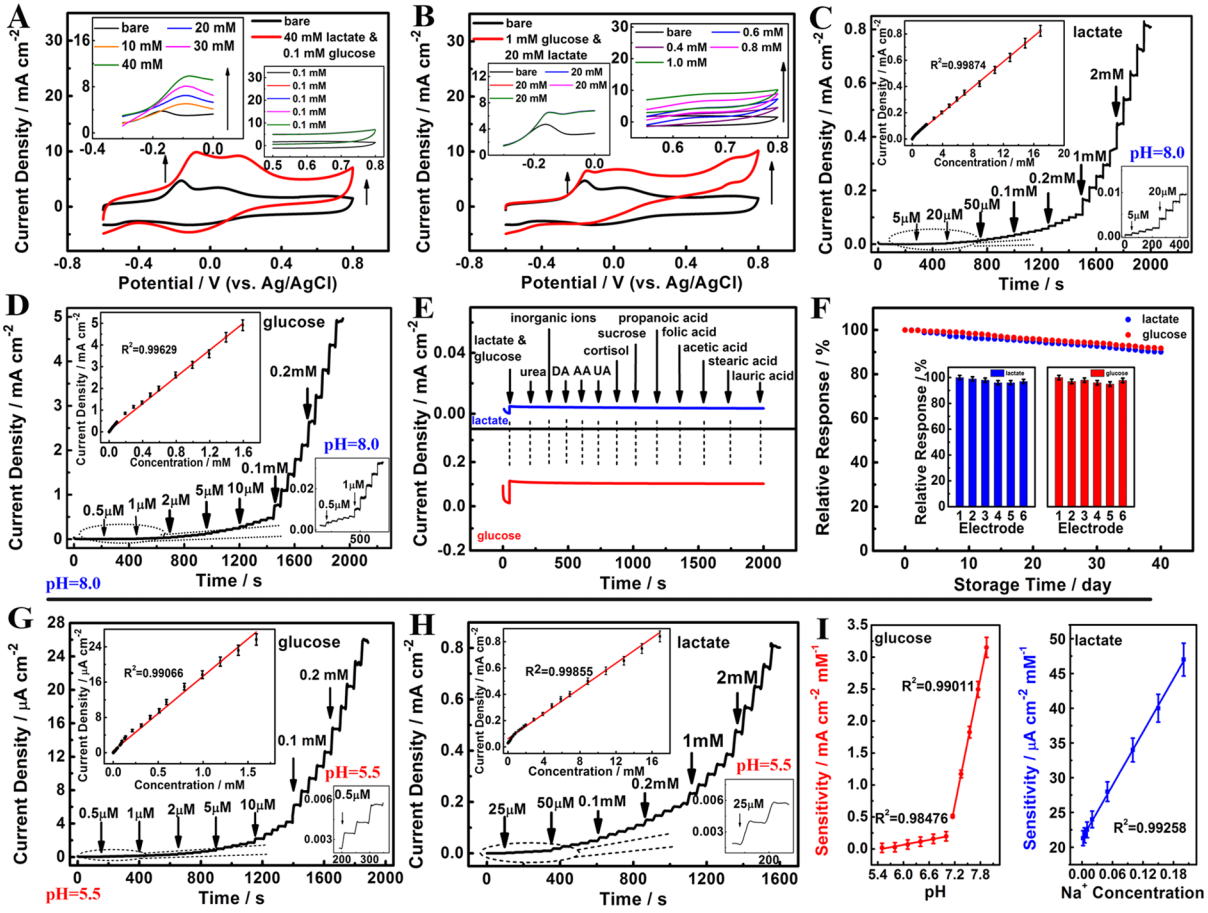

Figure 4. (A,B) Cyclic voltammogram of the **ACF-rGO/Cu(INA)$_2$** electrode in the simulated sweat (pH = 8.0) in the absence and presence of analytes at 50 mV/s. Inset: **ACF-rGO/Cu(INA)$_2$** linear sweep voltammetry curves. Current responses of the **ACF-rGO/Cu(INA)$_2$** electrode to successive injections of (C) lactate (−0.15 V) and (D) glucose (+0.62 V) in stirring simulated sweat (pH = 8.0). Inset: the corresponding calibration curve. (E) Effects of interferences on simultaneous detection. (F) Stability of the **ACF-rGO/Cu(INA)$_2$** electrode. Inset: response comparison with different **ACF-rGO/Cu(INA)$_2$** electrodes to 20 μM lactate and 20 μM glucose. Current responses of **ACF-rGO/Cu(INA)$_2$** to successive injections of (G) glucose (+0.62 V) and (H) lactate (−0.15 V) in stirring simulated sweat (pH = 5.5). Inset: corresponding calibration curve. (I) Calibration curve of sensitivity vs pH for glucose and C_{Na^+} for lactate.

$$E_{pa} = E^0 + \frac{RT}{(1-\alpha)nF} + \frac{RT}{(1-\alpha)nF}\ln v \quad (1)$$

$$E_{pc} = E^0 + \frac{RT}{\alpha nF} - \frac{RT}{\alpha nF}\ln v \quad (2)$$

where gas constant R (8.314 J mol^{-1} K^{-1}), Faraday constant F (96 500 C mol^{-1}), and temperature T (T = 298 K) are known quantities. According to the plots of E_{pa} and E_{pc} versus natural logarithm of the scan rate (ln v) (Figure 3D), for peaks I and II, α and n are calculated to be 0.60 and 1 and 0.42 and 1, respectively, demonstrating one-electron transfer. For totally irreversible diffusion-controlled behavior, the electron-transfer number could be computed based on the following equation[35]

$$|E_p - E_{p/2}| = \left(\frac{47.7}{\alpha n}\right) \quad (3)$$

α and n were estimated to be 0.66 and 1 for peak III, respectively. The electron-transfer rate k_s can be obtained from Laviron's theory when $n\Delta E_p$ > 200 mV[35]

$$k_s = \frac{\alpha nFv}{RT} \quad (4)$$

The value of k_s for Cu(0)/Cu(I), Cu(I)/Cu(II), and Cu(II)/Cu(III) are calculated as 1.59, 1.13, and 1.70 s^{-1}, respectively, at 50 mV s^{-1}. This result signifies fast electron transfer between ionic species and rime-structured Cu(INA)$_2$. Also, k_s for **ACF-rGO/Cu(INA)$_2$** is faster than that of some other representative Cu-based materials (see Figure S3).

Electrochemical Sensing Performances. Figure 4A,B represents a series of CV curves of the **ACF-rGO/Cu(INA)$_2$** microelectrode recorded in the simulated sweat electrolyte (pH = 8.0) containing different concentrations of lactate and glucose. Interestingly, **ACF-rGO/Cu(INA)$_2$** has the function to simultaneously detect lactate and glucose. The curves display a systematic increase of the oxidation peak current densities as the lactate and glucose concentrations increase, indicating that the **ACF-rGO/Cu(INA)$_2$** microelectrode possesses effective electrocatalytic oxidation activity toward lactate and glucose. Furthermore, when the glucose concentration is fixed, the corresponding response of the glucose remains unchanged and vice versa. This result demonstrates that response of lactate and glucose are separated and totally independent of each other. The potential of amperometric tests was optimized at −0.15 V (see optimization, from Figures S6−S9), and its corresponding i−t curves are depicted in Figure 4C. On aliquot injection of lactate, well-documented

DOI: 10.1021/acsami.8b07868
ACS Appl. Mater. Interfaces 2018, 10, 27936−27946

steady-state current responses are achieved within 5 s and the current densities increase stepwise. In the inset of Figure 4C, **ACF-rGO/Cu(INA)$_2$** demonstrates a linear dynamic concentration range of lactate from 5.0 μM to 16.875 mM, with the detection limit as low as 500 nM and sensitivity of 47 μA cm^{-2} mM^{-1} at a signal-to-noise (S/N) ratio of 3. Amperometric responses of **ACF-rGO/Cu(INA)$_2$** to successive concentration changes of glucose were tested at +0.62 V, and its corresponding $i-t$ curves are displayed in Figure 4D (see optimization, from Figures S10−S13). Moreover, the response of the **ACF-rGO/Cu(INA)$_2$** microelectrode rapidly reaches 95% of the steady-state value within 3 s upon each addition of glucose. A fine linear dependence on glucose concentration within the scope of 0.5−1592.5 μM can be achieved, with a detection limit down to 50 nM and a sensitivity of 3139.7 μA cm^{-2} mM^{-1} (S/N = 3) (inset of Figure 4D). The sensing performances of **ACF-rGO/Cu(INA)$_2$** are comparable or superior to those of previously reported lactate and glucose electrochemical sensors (see Table S1). For glucose sensing, **ACF-rGO/Cu(INA)$_2$** demonstrates higher sensitivity and lower detection limit along with a comparable linear range in comparison with other Cu-based materials. For lactate sensing, **ACF-rGO/Cu(INA)$_2$** exhibits higher sensitivity and lower detection limit as well as a wide linear range in comparison with nonenzymatic Cu-based and enzyme-based materials.

To investigate the anti-interference ability of **ACF-rGO/Cu(INA)$_2$**, the influence of some representative species, including Na^+, Cl^-, K^+, Mg^{2+}, Ca^{2+}, Al^{3+}, Zn^{2+}, NH_4^+, HCO_3^-, NO_3^-, SO_4^{2-}, CO_3^{2-}, I^-, IO_3^-, PO_4^{3-}, Li^+, Ba^{2+}, Mn^{2+}, Co^{2+}, Ni^{2+}, Br^-, F^-, HSO_4^-, HPO_4^{2-}, $H_2PO_4^-$ (10 mM), propanoic acid, folic acid, acetic acid, stearic acid, lauric acid (delspray), DA, AA, UA, urea, cortisol, and sucrose (1 μM), on the response of lactate and glucose was simultaneously evaluated at −0.15 and +0.62 V, respectively. Owing to nonelectroactivity of inorganic salt ions and no redox reaction of other organic small molecules on **ACF-rGO/Cu(INA)$_2$**, unconspicuous changes in the current response of lactate and glucose were observed (Figure 4E), implying excellent selectivity of the **ACF-rGO/Cu(INA)$_2$** microelectrode.

The stability of the proposed flexible microelectrode **ACF-rGO/Cu(INA)$_2$** with regard to its long-term stability, repeatability, and recyclability were investigated in detail. The results of the repeatability test exhibits that the relative standard deviation values of responses for six different **ACF-rGO/Cu(INA)$_2$** microelectrodes are less than 5% (inset of Figure 4F). As displayed in Figure 4F, the stability of the **ACF-rGO/Cu(INA)$_2$** microelectrode was estimated by repeatedly recording the amperometric response of the same **ACF-rGO/Cu(INA)$_2$** to 20 μM lactate and glucose. The results indicate that the response retains 92 and 91% of its initial value after storage for 40 days, which is attributed to the excellent stability of **ACF-rGO/Cu(INA)$_2$**. Furthermore, even if the microelectrode completely lost its activity after a long time, ACF-rGO can be reused as a recyclable substrate, and Cu(INA)$_2$ can be electrodeposited to obtain **ACF-rGO/Cu(INA)$_2$** again. These results reflect superb repeatability, long-term stability, and recyclability of the **ACF-rGO/Cu(INA)$_2$** microelectrode.

To the best of our knowledge, Cu-based materials are not useful for glucose detection in acid or neutral conditions because their sensing performances are dependent on the concentration of hydroxyl ions in the electrolyte. In our work, another charming finding is that **ACF-rGO/Cu(INA)$_2$** possesses the ability to measure glucose in acid medium. In the weak acid-simulated sweat (pH = 5.5), the current−time plots for the glucose of **ACF-rGO/Cu(INA)$_2$** are depicted in Figure 4G. **ACF-rGO/Cu(INA)$_2$** achieves 95% of the steady-state current within 5 s. It responds linearly to glucose up to 1592.5 μM, with a sensitivity of 16.3 μA cm^{-2} mM^{-1} and a detection limit of 0.1 μM (S/N = 3). To our surprise, these performances still sustain moderately compared with that in alkaline media. Under the same conditions, Figure 4H represents the steady-state currents toward lactate concentration. **ACF-rGO/Cu(INA)$_2$** exhibits a linear range of 25.0 μM to 16.875 mM (Figure 4H, inset) with a sensitivity of 46.8 μA cm^{-2} mM^{-1} and a detection limit of 0.5 μM (S/N = 3). This result indicates that the lactate-sensing performance is uncorrelated with pH of electrolyte. Figure 4I summarizes the linear relationship between the influencing factor and the sensitivity of the biosensor. Na-ion and OH-ion transfer process should, respectively, dominate the lactate and glucose determination ability of **ACF-rGO/Cu(INA)$_2$**. The mechanism for lactate and glucose oxidations can be represented as follows:

For lactate:

$$\{Cu^{II}INA\}_m + mNa^+ + me^- \rightarrow \{Cu^{I}(Na^+)INA\}_m \quad (5)$$

$$\{Cu^{I}(Na^+)INA\}_m + \text{lactate} + 2Na^+ \rightarrow \{Cu^{I}_{1-2/m}(Cu^0)_{2/m}(Na^+)_{1+2/m}INA\}_m + \text{pyruvate} \quad (6)$$

$$\{Cu^{I}_{1-2/m}(Cu^0)_{2/m}(Na^+)_{1+2/m}INA\}_m \rightarrow \{Cu^{I}(Na^+)INA\}_m + 2Na^+ + 2e^- \quad (7)$$

For glucose:

$$\{Cu^{II}INA\}_m + mH_2O \rightarrow \{Cu^{II}INA\cdot OH\}_m + me^- \quad (8)$$

$$2/m\{Cu^{III}INA\cdot OH\}_m + \text{glucose} \rightarrow 2/m\{Cu^{II}INA\}_m + \text{gluconolactone} \quad (9)$$

An important issue with **ACF-rGO/Cu(INA)$_2$** is the newly discovered ability to electro-oxidize lactate without using an enzyme. In **ACF-rGO/Cu(INA)$_2$**, electron hopping always occurs at adjacent Cu(I)/Cu(II) and Cu(II)/Cu(III) coupled with the ion diffusion of the charge-balancing electrolyte, making hopping extended across the entire nanorime. The diffusion of the cations is faster than that of electrons. This means Na(I) ions are relatively free to move across hierarchic channels of the nanorime MOFs, facilitating an efficient electron transfer. Na(I) cations spread along the rime interface into the inside very quickly. The previous oxidized centers (Cu(II)) along this interface are exhausted, and new oxidized centers (Cu(I)) expose to catalyze lactate, which is based upon the unhindered diffusion of both cations and electrons, loses its validity.

Another significant issue with **ACF-rGO/Cu(INA)$_2$** is the ability to determine glucose in acid media. Glucose-sensing performances in acid media is attributed to the following: in acid media, proton conduction in **ACF-rGO/Cu(INA)$_2$** typically occurs following the "vehicle mechanism" on account of the diffusion of the ionic carriers (H_3O^+).[2] During self-assembly of nanorime, because of the philic nature of the transition elements, Cu(II) is also coordinated to the nitrogen and oxygen donor atoms in NH_3 and H_2O, whereas some pyridine moieties in HINA are left free, which could act as the

DOI: 10.1021/acsami.8b07868
ACS Appl. Mater. Interfaces 2018, 10, 27936−27946

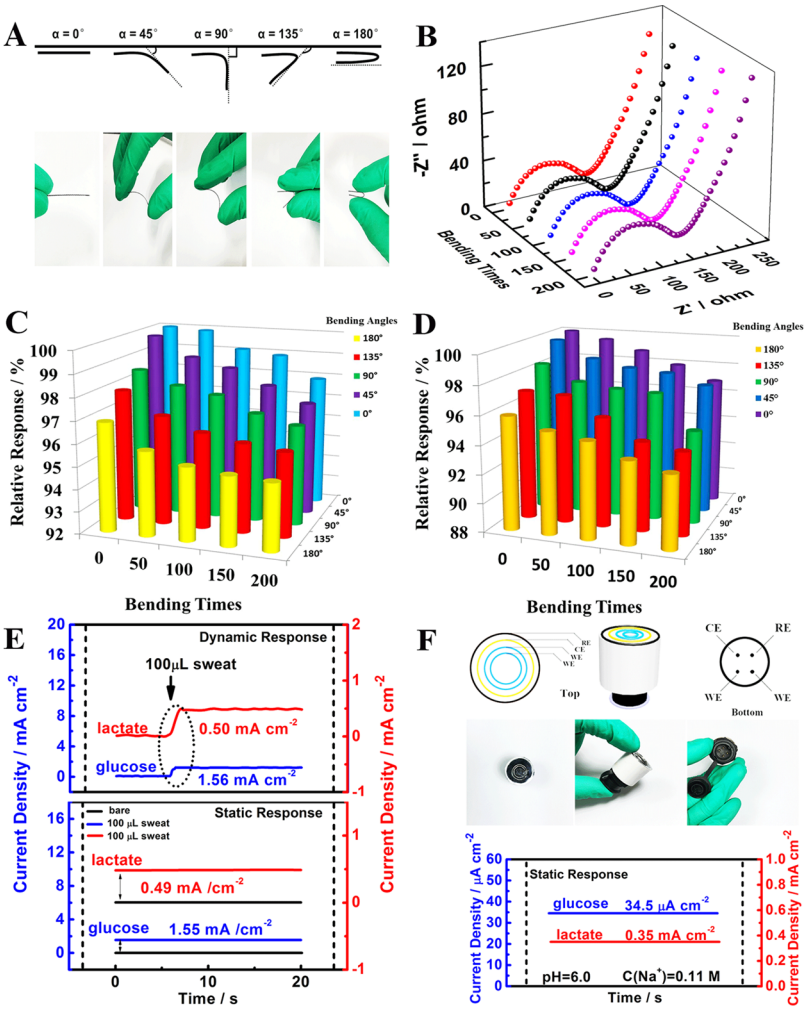

Figure 5. (A) Images of flexible **ACF-rGO/Cu(INA)$_2$**. (B) EIS curves of **ACF-rGO/Cu(INA)$_2$** after repetitive bending. Bar graphs of bending times and angles effects of **ACF-rGO/Cu(INA)$_2$** in response to 0.02 mM (C) lactate and (D) glucose. (E) Current response, using **ACF-rGO/Cu(INA)$_2$**, to real perspiration. (F) Images of **ACF-rGO/Cu(INA)$_2$**-based platform and current response to real sweat-using platform.

Lewis basic sites. Therefore, unsaturated nitrogen atoms in MOFs are preferably combined with the proton. Nanorime offers an intrinsic advantage in this regard because its multistage porous nature makes it easy to incorporate the desired proton close to their active sites, creating a relatively alkaline microenvironment. Moreover, dense, open, and unsaturated metal sites originating from the removal of NH_3 and H_2O molecules during the drying process will absorb OH^- fast, driven by their high surface energy. Thus, hydroxyl radicals are produced at the Cu(III) catalytic center under a high potential window.

On the basis of the abovementioned evaluation of electrochemical sensing performance, another question arises: why does nanorime-structured **ACF-rGO/Cu(INA)$_2$** possess outstanding sensing ability? It is attributed to the improved conductivity and activity derived from the rational rime-structured design. Transfer of ions and electrons play a crucial role in sensing performances, whatever the lactate and glucose responses for **ACF-rGO/Cu(INA)$_2$**. Murray's law manifests that the porous network within a confined volume would minimize the transport resistance and enable fluent transfer throughout the whole network.[36] In **ACF-rGO/Cu(INA)$_2$**, for mass and diffusion and ionic or electronic transfer

$$Q_1 = D\pi r^2 \frac{\Delta C}{l} \tag{10}$$

$$Q_2 = \sigma\pi r^2 \frac{\Delta V}{l} \tag{11}$$

We define that Q_1 and Q_2 are, respectively, the amount of analytes and electrons diffused through a cross-section per unit time; D and σ are, respectively, the diffusion coefficient and conductivity through a cross-section per unit time, y; ΔC and ΔV are the concentration and potential difference across the pore, respectively. A Lagrange multiplier λ is introduced to minimize the entransy dissipation rate according to Murray's principle

$$\frac{\partial(Q_1\Delta C - \lambda V)}{\partial r} = 0 \tag{12}$$

$$\frac{\partial(Q_2\Delta V - \lambda V)}{\partial r} = 0 \tag{13}$$

We can obtain $Q_1 = k_1 r^2$, $Q_2 = k_2 r^2$, where k_1 and k_2 are constants (see details in the Supporting Information). Therefore, for connecting macropores with radius of r to

DOI: 10.1021/acsami.8b07868
ACS Appl. Mater. Interfaces 2018, 10, 27936−27946

subpores with radius of r_i for mass, electron, or ion transfer with considering mass and electrons, the law gives

$$Q_m = \sum_{i=1}^{N} Q_i \quad (14)$$

$$r^2 = \sum_{i=1}^{N} r_i^2 \quad (15)$$

where Q_m is the amount of substances imported into the macropores or the electrons and ions transferred through the cross-section per unit time. On the basis of the derivation of formula, Q_m is proportional to the reaction rate. Further, eq 15 further reveals that the diffusion rate of analytes, Na^+, and electrons depends on the size and distribution of pores. A space-filling and branching network in the rime structure following Murray's law endows **ACF-rGO/Cu(INA)$_2$** with a larger surface area for analyte adsorption and fast diffusion. Multilevel pores provide a high surface to volume ratio and reduce the diffusion time of mass transport, thus enhancing the detection capability of **ACF-rGO/Cu(INA)$_2$**. Also, the porous rime-structured MOF film that allows for nanoconfinement of lactate and glucose improves the electron-transfer kinetics inside the multilevel pores. More importantly, the rime structure also brings about a favorable microenvironment for Na(I) ion transfer and proton immobilization. On the other hand, nanoporous surface environments bring about a "macromolecular crowding" phenomenon, simulating excluded volume effect and further enhancing the stability of biomolecules captured inside a nanopore.[37] Also, porous surfaces provide size-based exclusion, reducing the noise from the environment, which increases selectivity.

Flexibility Tests and Real Sweat Evaluation. Flexible, wearable sweat-sensing devices are essential for the realization of personalized treatment, yielding significant information available from biomarkers about the underlying physiology of individuals for real-time monitoring of health.[38−43] As one of the two foremost biomarkers in human perspiration, sweat lactate always represents the restricted oxidative metabolism and compromise of tissue viability, offering warning for insufficient blood flow. Hence, it is used to track the exertion level of a human subject (10 times as much as that in blood).[44,45] Sweat glucose (0.28−1.11 mM) has been discovered and confirmed to be related to blood glucose, the concentration of which is 4−8 mM.[46,47] On the basis of these characteristics, the working platform for the biofunctionally measurement of lactate and glucose would be an indispensable part of wearable sweat sensors and will have access to abundant information about user's physiological and metabolic states.

Flexibility is significant in the construction of biomedical electronics and miniaturized wearable devices for in vitro and in vivo biomarker monitoring.[48−50] Therefore, the influences of mechanical stress induced by bending on **ACF-rGO/Cu(INA)$_2$** microelectrode performance have been investigated. Our results show that bending inward 180° for 200 times has no effects on the resistance behavior of **ACF-rGO/Cu(INA)$_2$** (Figure 5B). As shown in Figure 5C,D, the effects of the different bending times and angles reflect comprehensive information for flexibility. With the increase of the bending angles and bending times, the relative response showed an overall downward trend. Upon bending inward for different bending times from 45° to 180° angles (Figure 5A), the flexible **ACF-rGO/Cu(INA)$_2$** microelectrode exhibits a minor change (95.1 and 93.6%) in the amperometric response to 20 μM lactate and 20 μM glucose, respectively. This result demonstrates that repetitive bending makes no difference to lactate and glucose sensing. It demonstrates that the electrochemical behaviors of **ACF-rGO/Cu(INA)$_2$** are independent of the bending states.

ACF-rGO/Cu(INA)$_2$ is further employed to be a biofunctional sensing platform for simultaneous sweat lactate and glucose detection. A healthy volunteer was recruited for participation in the sweat study. Simulated sweat (pH = 8.0, without lactate and glucose) was used as the electrolyte; the sensor was mounted on an electrochemical workstation with dual channels, and the output was set as −0.15 and +0.62 V. A representative experimental result is shown in Figure 5E. The concentrations of lactate and glucose calculated by calibration curve equations in the sample were 10.01 and 0.51 mM, respectively. Sweat information extracted from the current response data was within the normal resting range. Further, static measurement is further employed to examine the real performance of **ACF-rGO/Cu(INA)$_2$**. The result indicates that a tiny difference can be negligible even the performance will degrade when microelectrode is used to work in situ manner. Typical and standard ultraviolet (UV) spectrophotometry also has been utilized to correlate and validate the sweat-sensing performances of **ACF-rGO/Cu(INA)$_2$** nanorime (see UV correlation and validation in the Supporting Information). It demonstrates that our electrochemical analysis to sweat lactate and glucose is credible.

Motivated by the superb sensing performances, we introduce a simple platform composed of a three-electrode amperometric lactate and glucose biosensor, enabling testing to validate the performance of **ACF-rGO/Cu(INA)$_2$**. The hybrid-sensing platform was fabricated leveraging a simple package of two microelectrodes, Ag/AgCl, and Pt as the working, reference, and counter electrodes on an insulating polyester sheet (see details in the Supporting Information). In the same way, static tests were carried out for the simultaneous analysis of the same sweat sample (pH = 6.0, C_{Na^+} = 0.11 M) without using an electrolyte to avoid dilution. As displayed in Figure 5F, the real sweat lactate and glucose responses based on the device are 0.35 mA cm^{-2} and 34.5 μA cm^{-2}, respectively. According to the relationship between sensitivity and variables (Figure 4I), the sweat lactate and glucose are calculated to be 9.99 and 0.50 mM, respectively. This result illustrates that sweat can be directly tested, which is essential for wearable sweat devices. For achieving more accurate chemical responses in a real-time manner, an advanced wireless system is necessary to be introduced with the biosensor, which will be the next step in exploring wearable electronics.

CONCLUSIONS

We report a nanorime MOF film with new functionalities via a simple, generalized, and eco-friendly electrochemical approach. This rime-inspired approach leads to in situ simultaneous assembly onto the desired surface of the ACF, which allows us to achieve aligned rime-structured MOFs with uniform hierarchical pores. Our strategy bridges biomineralization and electrochemical-induced self-assembly of MOFs and captures their inner similarity, providing new insights into fabrication of MOF films. The suitable surface design offers fast diffusion of analytes and enhanced electron-transfer kinetics and makes the MOF film an ideal entrant in nonenzymatic sweat biosensing for the first time. We believe that the electrochemical interface-

DOI: 10.1021/acsami.8b07868
ACS Appl. Mater. Interfaces 2018, 10, 27936−27946

induced approach for the synthesis of rime-structured MOFs can bring about a beneficial foundation and novel thinking for the design and modification of novel types of biomimetic MOF-based sensing devices and systems. We envision that the wireless electronic technology and predictive algorithms, based on large data mining techniques, along with our biomimetic technique, would open up new horizons for a better understanding of the health status of humans and pave new avenues for the practical application of MOF-based wearable devices.

■ ASSOCIATED CONTENT

Supporting Information

The Supporting Information is available free of charge on the ACS Publications website at DOI: 10.1021/acsami.8b07868.

Crystal structures of $Cu(INA)_2$; preparation method of bulk $Cu(INA)_2$; comparison of k_s with other Cu-based materials; effect of different structures on the performance; optimization of conditions for lactate detection; optimization of conditions for glucose detection; recycling property of ACF-rGO/$Cu(INA)_2$; stability and reproducibility of ACF-rGO/$Cu(INA)_2$ in acid media; CV response of bulk $Cu(INA)_2$; sensing performances of reported analogue electrochemical biosensors; Murray's principle; and procedures of sweat test and UV spectrophotometry correlation and validation (PDF)

■ AUTHOR INFORMATION

Corresponding Author

*E-mail: liuhf@hust.edu.cn.

ORCID

Fei Xiao: 0000-0002-7081-1998

Hongfang Liu: 0000-0002-9180-6629

Author Contributions

The manuscript was written through contributions of all authors. All authors have given approval to the final version of the manuscript.

Notes

The authors declare no competing financial interest.

■ ACKNOWLEDGMENTS

This research is supported by the National Natural Science Foundation of China (project no. U1662114), the Independent Innovation Research Fund of Huazhong University of Science and Technology (2017KFYXJJ164), the Foundation of Hubei Key Laboratory of Material Chemistry and Service Failure (no. 201502, 201702), and the Key Laboratory of Material Chemistry for Energy Conversion and Storage, Ministry of Education (2018).

■ REFERENCES

(1) Doonan, C.; Riccò, R.; Liang, K.; Bradshaw, D.; Falcaro, P. Metal-Organic Frameworks at the Biointerface: Synthetic Strategies and Applications. *Acc. Chem. Res.* **2017**, *50*, 1423−1432.

(2) Stassen, I.; Burtch, N.; Talin, A.; Falcaro, P.; Allendorf, M.; Ameloot, R. An updated roadmap for the integration of metal-organic frameworks with electronic devices and chemical sensors. *Chem. Soc. Rev.* **2017**, *46*, 3185−3241.

(3) Knebel, A.; Zhou, C.; Huang, A.; Zhang, J.; Kustov, L.; Caro, J. Smart Metal-Organic Frameworks (MOFs): Switching Gas Permeation through MOF Membranes by External Stimuli. *Chem. Eng. Technol.* **2018**, *41*, 224−234.

(4) Wu, M.-X.; Yang, Y.-W. Metal-Organic Framework (MOF)-Based Drug/Cargo Delivery and Cancer Therapy. *Adv. Mater.* **2017**, *29*, 1606134.

(5) Duan, J.; Chen, S.; Zhao, C. Ultrathin Metal-Organic Framework Array for Efficient Electrocatalytic Water Splitting. *Nat. Commun.* **2017**, *8*, 15341.

(6) Huang, Y.-B.; Liang, J.; Wang, X.-S.; Cao, R. Multifunctional Metal-Organic Framework Catalysts: Synergistic Catalysis and Tandem Reactions. *Chem. Soc. Rev.* **2017**, *46*, 126−157.

(7) He, H.; Perman, J. A.; Zhu, G.; Ma, S. Metal-Organic Frameworks for CO2Chemical Transformations. *Small* **2016**, *12*, 6309−6324.

(8) Alizadeh, S.; Nematollahi, D. Electrochemically Assisted Self-Assembly Technique for the Fabrication of Mesoporous Metal-Organic Framework Thin Films: Composition of 3D Hexagonally Packed Crystals with 2D Honeycomb-like Mesopores. *J. Am. Chem. Soc.* **2017**, *139*, 4753−4761.

(9) Liu, J.; Wöll, C. Surface-Supported Metal-Organic Framework Thin Films: Fabrication Methods, Applications, and Challenges. *Chem. Soc. Rev.* **2017**, *46*, 5730−5770.

(10) Stavila, V.; Schneider, C.; Mowry, C.; Zeitler, T. R.; Greathouse, J. A.; Robinson, A. L.; Denning, J. M.; Volponi, J.; Leong, K.; Quan, W.; Tu, M.; Fischer, R. A.; Allendorf, M. D. Thin Film Growth of Nbo MOFs and Their Integration with Electro-acoustic Devices. *Adv. Funct. Mater.* **2016**, *26*, 1699−1707.

(11) Sachdeva, S.; Venkatesh, M. R.; Mansouri, B. E.; Wei, J.; Bossche, A.; Kapteijn, F.; Zhang, G. Q.; Gascon, J.; de Smet, L. C. P. M.; Sudhölter, E. J. R. Sensitive and Reversible Detection of Methanol and Water Vapor by in Situ Electrochemically Grown CuBTC MOFs on Interdigitated Electrodes. *Small* **2017**, *13*, 1604150.

(12) Qiu, X.; Wang, X.; Li, Y. Controlled Growth of Dense and Ordered Metal-Organic Framework Nanoparticles on Graphene Oxide. *Chem. Commun.* **2015**, *51*, 3874−3877.

(13) Carné, A.; Carbonell, C.; Imaz, I.; Maspoch, D. Nanoscale Metal-Organic Materials. *Chem. Soc. Rev.* **2011**, *40*, 291−305.

(14) Tanaka, D.; Henke, A.; Albrecht, K.; Moeller, M.; Nakagawa, K.; Kitagawa, S.; Groll, J. Rapid Preparation of Flexible Porous Coordination Polymer Nanocrystals with Accelerated Guest Adsorption Kinetics. *Nat. Chem.* **2010**, *2*, 410−416.

(15) Chen, N.; Dai, Y.; Xing, Y.; Wang, L.; Guo, C.; Chen, R.; Guo, S.; Wu, F. Biomimetic Ant-Nest Ionogel Electrolyte Boosts the Performance of Dendrite-Free Lithium Batteries. *Energy Environ. Sci.* **2017**, *10*, 1660−1667.

(16) Baik, S.; Kim, D. W.; Park, Y.; Lee, T.-J.; Bhang, S. H.; Pang, C. A Wet-Tolerant Adhesive Patch Inspired by Protuberances in Suction Cups of Octopi. *Nature* **2017**, *546*, 396−400.

(17) Rodenas, T.; Luz, I.; Prieto, G.; Seoane, B.; Miro, H.; Corma, A.; Kapteijn, F.; Llabrés i Xamena, F. X.; Gascon, J. Metal-Organic Framework Nanosheets in Polymer Composite Materials for Gas Separation. *Nat. Mater.* **2015**, *14*, 48−55.

(18) Yoo, Y.; Jeong, H.-K. Rapid Fabrication of Metal Organic Framework Thin Films Using Microwave-Induced Thermal Deposition. *Chem. Commun.* **2008**, 2441−2443.

(19) Biemmi, E.; Scherb, C.; Bein, T. Oriented Growth of the Metal Organic Framework Cu3(BTC)2(H2O)3·xH2O Tunable with Functionalized Self-Assembled Monolayers. *J. Am. Chem. Soc.* **2007**, *129*, 8054−8055.

(20) Shekhah, O.; Wang, H.; Kowarik, S.; Schreiber, F.; Paulus, M.; Tolan, M.; Sternemann, C.; Evers, F.; Zacher, D.; Fischer, R. A.; Wöll, C. Step-by-Step Route for the Synthesis of Metal−Organic Frameworks. *J. Am. Chem. Soc.* **2007**, *129*, 15118−15119.

(21) Ameloot, R.; Gobechiya, E.; Uji-i, H.; Martens, J. A.; Hofkens, J.; Alaerts, L.; Sels, B. F.; De Vos, D. E. Direct Patterning of Oriented Metal-Organic Framework Crystals via Control over Crystallization Kinetics in Clear Precursor Solutions. *Adv. Mater.* **2010**, *22*, 2685−2688.

(22) Schoedel, A.; Scherb, C.; Bein, T. Oriented Nanoscale Films of Metal-Organic Frameworks By Room-Temperature Gel-Layer Synthesis. *Angew. Chem., Int. Ed.* **2010**, *49*, 7225−7228.
(23) Estroff, L. A. Introduction: Biomineralization. *Chem. Rev.* **2008**, *108*, 4329−4331.
(24) Liang, K.; Ricco, R.; Doherty, C. M.; Styles, M. J.; Bell, S.; Kirby, N.; Mudie, S.; Haylock, D.; Hill, A. J.; Doonan, C. J.; Falcaro, P. Biomimetic Mineralization of Metal-Organic Frameworks as Protective Coatings for Biomacromolecules. *Nat. Commun.* **2015**, *6*, 7240.
(25) Rathee, K.; Dhull, V.; Dhull, R.; Singh, S. Biosensors Based on Electrochemical Lactate Detection: A Comprehensive Review. *Biochem. Biophys. Rep.* **2016**, *5*, 35−54.
(26) Nery, E. W.; Kundys, M.; Jeleń, P. S.; Jönsson-Niedziółka, M. Electrochemical Glucose Sensing: Is There Still Room for Improvement? *Anal. Chem.* **2016**, *88*, 11271−11282.
(27) Mao, J.; Ge, M.; Huang, J.; Lai, Y.; Lin, C.; Zhang, K.; Meng, K.; Tang, Y. Constructing Multifunctional MOF@rGO Hydro-/Aerogels by the Self-Assembly Process for Customized Water Remediation. *J. Mater. Chem. A* **2017**, *5*, 11873−11881.
(28) Al-Kutubi, H.; Gascon, J.; Sudhölter, E. J. R.; Rassaei, L. Electrosynthesis of Metal-Organic Frameworks: Challenges and Opportunities. *ChemElectroChem* **2015**, *2*, 462−474.
(29) Campagnol, N.; Van Assche, T. R. C.; Li, M.; Stappers, L.; Dincă, M.; Denayer, J. F. M.; Binnemans, K.; De Vos, D. E.; Fransaer, J. On the Electrochemical Deposition of Metal-Organic Frameworks. *J. Mater. Chem. A* **2016**, *4*, 3914−3925.
(30) Li, W.-J.; Tu, M.; Cao, R.; Fischer, R. A. Metal-organic framework thin films: electrochemical fabrication techniques and corresponding applications & perspectives. *J. Mater. Chem. A* **2016**, *4*, 12356−12369.
(31) Wang, W.; Liu, W.; Zeng, Y.; Han, Y.; Yu, M.; Lu, X.; Tong, Y. A Novel Exfoliation Strategy to Significantly Boost the Energy Storage Capability of Commercial Carbon Cloth. *Adv. Mater.* **2015**, *27*, 3572−3578.
(32) Lin, X.; Ni, Y.; Kokot, S. Electrochemical and bio-sensing platform based on a novel 3D Cu nano-flowers/layered MoS 2 composite. *Biosens. Bioelectron.* **2016**, *79*, 685−692.
(33) Huang, X.; Sheng, P.; Tu, Z.; Zhang, F.; Wang, J.; Geng, H.; Zou, Y.; Di, C.-a.; Yi, Y.; Sun, Y.; Xu, W.; Zhu, D. A Two-Dimensional π-d Conjugated Coordination Polymer with Extremely High Electrical Conductivity and Ambipolar Transport Behaviour. *Nat. Commun.* **2015**, *6*, 7408.
(34) Bard, A. J. *Electrochemical Methods. Fundamentals and Applications*; Wiley, Vol *96*; 2001.
(35) Laviron, E. General Expression of the Linear Potential Sweep Voltammogram in the Case of Diffusionless Electrochemical Systems. *J. Electroanal. Chem. Interfacial Electrochem.* **1979**, *101*, 19−28.
(36) Zheng, X.; Shen, G.; Wang, C.; Li, Y.; Dunphy, D.; Hasan, T.; Brinker, C. J.; Su, B.-L. Bio-inspired Murray materials for mass transfer and activity. *Nat. Commun.* **2017**, *8*, 14921.
(37) Munje, R. D.; Muthukumar, S.; Prasad, S. Lancet-Free and Label-Free Diagnostics of Glucose in Sweat Using Zinc Oxide Based Flexible Bioelectronics. *Sens. Actuators, B* **2017**, *238*, 482−490.
(38) Anastasova, S.; Crewther, B.; Bembnowicz, P.; Curto, V.; Ip, H. M. D.; Rosa, B.; Yang, G.-Z. A Wearable Multisensing Patch for Continuous Sweat Monitoring. *Biosens. Bioelectron.* **2017**, *93*, 139−145.
(39) Gao, W.; Emaminejad, S.; Nyein, H. Y. Y.; Challa, S.; Chen, K.; Peck, A.; Fahad, H. M.; Ota, H.; Shiraki, H.; Kiriya, D.; Lien, D.-H.; Brooks, G. A.; Davis, R. W.; Javey, A. Fully Integrated Wearable Sensor Arrays for Multiplexed in Situ Perspiration Analysis. *Nature* **2016**, *529*, 509−514.
(40) Nakata, S.; Arie, T.; Akita, S.; Takei, K. Wearable, Flexible, and Multifunctional Healthcare Device with an ISFET Chemical Sensor for Simultaneous Sweat pH and Skin Temperature Monitoring. *ACS Sens.* **2017**, *2*, 443−448.
(41) Wang, S.; Wu, Y.; Gu, Y.; Li, T.; Luo, H.; Li, L.-H.; Bai, Y.; Li, L.; Liu, L.; Cao, Y.; Ding, H.; Zhang, T. Wearable Sweatband Sensor Platform Based on Gold Nanodendrite Array as Efficient Solid Contact of Ion-Selective Electrode. *Anal. Chem.* **2017**, *89*, 10224.
(42) Deng, Z.; Jiang, H.; Hu, Y.; Liu, Y.; Zhang, L.; Liu, H.; Li, C. 3D Ordered Macroporous MoS2 @C Nanostructure for Flexible Li-Ion Batteries. *Adv. Mater.* **2017**, *29*, 1603020.
(43) Dam, V. A. T.; Zevenbergen, M. A. G.; van Schaijk, R. Toward Wearable Patch for Sweat Analysis. *Sens. Actuators, B* **2016**, *236*, 834−838.
(44) Derbyshire, P. J.; Barr, H.; Davis, F.; Higson, S. P. J. Lactate in Human Sweat: a Critical Review of Research to the Present Day. *J. Physiol. Sci.* **2012**, *62*, 429−440.
(45) Onor, M.; Gufoni, S.; Lomonaco, T.; Ghimenti, S.; Salvo, P.; Sorrentino, F.; Bramanti, E. Potentiometric sensor for non invasive lactate determination in human sweat. *Anal. Chim. Acta* **2017**, *989*, 80−87.
(46) Wang, Z.; Dong, S.; Gui, M.; Asif, M.; Wang, W.; Wang, F.; Liu, H. Graphene paper supported MoS 2 nanocrystals monolayer with Cu submicron-buds: High-performance flexible platform for sensing in sweat. *Anal. Biochem.* **2018**, *543*, 82−89.
(47) Talary, M. S.; Dewarrat, F.; Huber, D.; Caduff, A. In Vivo Life Sign Application of Dielectric Spectroscopy and Non-Invasive Glucose Monitoring. *J. Non-Cryst. Solids* **2007**, *353*, 4515−4517.
(48) Wang, L.; Dong, Y.; Zhang, Y.; Zhang, Z.; Chi, K.; Yuan, H.; Zhao, A.; Ren, J.; Xiao, F.; Wang, S. PtAu Alloy Nanoflowers on 3D Porous Ionic Liquid Functionalized Graphene-Wrapped Activated Carbon Fiber as a Flexible Microelectrode for Near-Cell Detection of Cancer. *NPG Asia Mater.* **2016**, *8*, No. e337.
(49) Xiao, F.; Wang, L.; Duan, H. Nanomaterial Based Electrochemical Sensors for In Vitro Detection of Small Molecule Metabolites. *Biotechnol. Adv.* **2016**, *34*, 234−249.
(50) Wang, Z.; Gui, M.; Asif, M.; Yu, Y.; Dong, S.; Wang, H.; Wang, W.; Wang, F.; Xiao, F.; Liu, H. A Facile Modular Approach to the 2D Oriented Assembly MOF Electrode for Non-Enzymatic Sweat Biosensors. *Nanoscale* **2018**, *10*, 6629−6638.

DOI: 10.1021/acsami.8b07868
ACS Appl. Mater. Interfaces 2018, 10, 27936−27946